CHAPTER 4
POOL BOILING HEAT TRANSFER ON HORIZONTAL MINI-FINNED SURFACES IN SATURATED FC-72

The pool boiling heat transfer and associated vapor/bubble characteristics of dielectric fluid FC-72 on horizontal finned surfaces are inspected in this chapter. The experiments are conducted for the saturated temperature 56.6   (corresponding to the FC-72 saturated pressure 1 atm). The finned surfaces with four fin length (0.5, 1.0, 2.0, and 4.0mm) and three fin spacing (0.5, 1.0, and 2.0mm) which fabricated on a 10mm×10mm base area are immersed in saturated FC-72 for this study. The heat transfer characteristics of the FC-72 pool boiling are expressed in terms of the boiling curves in which the plots of the heat flux versus the wall superheat for various fin spacing and fin length are depicted. Moreover, selected experimental data and flow pattern photos from the present study are presented to illustrate the pool boiling heat transfer coefficient and associated vapor/bubble behavior including bubble departure mechanism and bubble interaction.

4.1 Visual Flow Pattern Observation of Mini-Finned Surface

Progressive photographic observations are used to investigate the effects of geometry parameters with the heat flux from 1×10^4 Wm^{-2} to 9.5×10^5 Wm^{-2}. Figure 4.1 shows the flow pattern images of twelve finned surfaces at boiling incipience. As the boiling is initiated, the bubbles are generated from some active nucleate sites of the fins and a large portion of the test surface remains under free convection condition. An interesting phenomenon observed is that initial boiling occurs at some particular locations – typically at the fin tip, whence it spreads to the fin root, regardless of whether the wall superheat at the fin root is exceeded that at the fin tip. Unlike the bubbles that depart from the fin tip and can freely flow upward, the departure bubbles from the fin root may be easily trapped at the corner of fin root momentarily without leaving. Additionally, the induced convective motion of the fluid flow may also reduce the size of trapped bubbles.

As pointed out by Cole [53], the departure bubble diameter D_d can be expressed in terms of the Bond number. Bo . , as,

$$D_d = \left(\frac{Bo\sigma}{g(\rho_l - \rho_v)} \right)^{0.5}$$

(4-1)

where Bo is given by Cole [53],

$$Bo = (0.04Ja)^2$$

(4-2)

and

$$Ja = \left(\frac{\rho_l Cp_l \Delta T_{sat}}{\rho_v i_{lv}} \right)$$

(4-3)

For the dielectric FC-72 fluid tested under atmospheric condition, the departure diameter is estimated to be around 0.2 ~ 0.3mm. The estimated bubble departure diameter is verified by observation herein and that by Rini et al. [66]. For another dielectric fluid, HFE7100, a corresponding value of 0.55mm is obtained by EL-Genk et al. [65].

Figure 4.2 shows that the number of active nucleate sites and the bubble departure frequency increases with a small rise in heat flux. The boiling regions gradually spread from the fin tip to the fin root. The figures also indicate that some bubbles begin to impact the adjacent fin and activate the non-active cavities thereon. Moreover, the flow patterns show that active nucleate cavities exist distinctly and bubbles depart without interaction in low heat flux region. The departure bubble diameter observed herein are still maintains at 0.2 ~ 0.3mm.

The flow patterns displayed in Figure 4.3 are obtained from twelve different finned surfaces boiling in the moderate heat flux region. The figures reveal a sharp rise in nucleation density and departure frequency. In Figures 4.3(a) to (h), a large number of bubbles are generated from side surfaces of fins and also cover entire fin surface. Moreover, bubbles generated from the side surface of fins begin to detach from or slid along the fin. The interactions and coalescence of bubbles are also observed in the closer spacing between adjacent fins. These mechanisms induce flow resistance against the lift-off bubbles along the

fin. Flow resistance also delays the departure bubbles generated from the fin root and causes the bubbles to coalesce inside fin spacing during the longer lift-off time. Figure 4.3(i) to (l) present the flow patterns of the surface with the fins more widely spaced S=2mm. Unlike the more compact fin array in which bubbles interfere with each other inside fin spacing, the boiling mechanisms of the rarer fin array are more similar to those on the isolated fin. The departure bubble diameter observed herein ranges from 0.3 to 0.5mm.

When the heat flux approach to CHF as shown in Figure 4.4, a short periodical vapor mushroom departure process is observed and large vapor mushroom clouds are found to accumulate inside the fin spacing before splitting into several vapor clouds prior to lift-off. In Figure 4.4(c), (d) and (h), larger flow resistance along the narrower spacing and longer fin length results parts of vapor mushroom clouds extruded from the perimeter of the fin array. This periodical departure process may obstruct and may delay the re-wetting liquid entering the fin array, finally causing temporary dry-out in the center of the fin array and rapid rising the wall superheat, leading to critical heat flux.
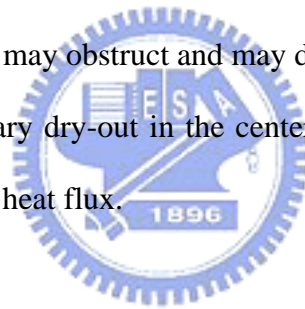
4.2 The Effects of the Geometric Parameter on Boiling Heat Transfer Performance

4.2.1 Boiling Incipience Superheat and CHF

The boiling incipience superheat and CHF value of the finned surfaces with various fin spacing are schematically depicted in Figures 4.5, 4.6, and 4.7. The figures plot the conventional boiling curves (q_b'' versus ΔT) with increasing heat flux. The test results obtained from plain surface is also plotted for comparison. The data indicate that, for all finned surfaces, the boiling incipience superheat are approximately 7~11K and the temperature excursions of hysteresis are about 1~3K. The boiling hysteresis wall superheat of finned surfaces is obviously less than that of the plain surface (27.32K). Table 4.1 presents the average boiling incipience superheat (5 test runs) with various fin spacing and lengths. The boiling incipience superheat decreases as the fin length increases or fin spacing decreases, due to the

much larger fin surface area the more nucleate sites. Moreover, the temperature excursion is also eliminated with more compact finned surface.

As the boiling is initiated, the bubbles are generated from some locations of the finned surface and a large portion of the surface is still in the natural convection condition. When the boiling regions spread, the temperature excursion of wall superheat is constantly maintained and boiling curve shows a vibrating behavior on wall superheat which is different from the plain surface. Hence, compared with the high hysteresis of the plain surface, the boiling hysteresis of the finned surfaces are relatively indistinct. Until the entire surface is in boiling condition, the superheat eventually increased with the heat flux.

The CHF value ($q''_{b,CHF}$) versus fin spacing and fin length as presented in Figure 4.8. Increasing the heat transfer area per unit base surface increases heat dissipation when the fins are closer or higher. The reduction of the fin spacing indicates the increase of the numbers of fins and the wetting area. The increase in fin length can also increase the wetting area. Hence, the closer fins (more compact fin array) and higher fins can provide more wetting area for boiling. The Figure shows that the CHF values are raised as the increase in fin length or reduce in fin spacing. Moreover, it is clear to note that the effect of the fin length on CHF is more significant than that of fin spacing.

4.2.2 Boiling Heat Transfer Coefficient on Horizontal Mini-finned Surfaces

The plots of Figure 4.9, 4.10 and 4.11 illustrate the changes of overall boiling heat transfer coefficient on copper finned surfaces with overall heat flux for various fin spacing and lengths. At a larger fin spacing of S=2mm shown in Figure 4.9, the slopes of the boiling curves are approximately the same in the region $q''_t < 5 \times 10^4$ Wm^{-2}, independently of the lengths of the fins. However, the larger fin lengths yield lower overall heat transfer coefficients in moderate and high heat flux regions in $q''_t > 5 \times 10^4$ Wm^{-2}. It is obviously due to the effect of flow resistance to

departure bubble and superheated liquid with increasing fin length. The photo images in Figure 4.3(i) and (j) indicate that bubbles either lift-off directly from the fin tip and base surface or slide for a short distance along the fins. However, for the longer fin arrangements observed in Figure 4.3(k) and (l), a large number of bubbles generate from the side surfaces of fins and slide along the fins before they detach from the fins. Those sliding bubbles may obstruct the lift-off bubbles departing from the fin root and base surface. Similar behavior is further noticeable in smaller spacing of S=0.5mm and S=1mm as shown in Figure 4.3(c), (d), (g) and (h). Therefore, at a smaller fin spacing of S=0.5mm as shown in Figure 4.11, the slopes of the boiling curves change considerably with the fin length in the region $q_t'' > 1.6 \times 10^4$ Wm^{-2}. The results further verify that increasing the fin length or decreasing the fin spacing can enhance the resistance against bubble departure.

The plots in 4.9, 4.10 and 4.11 also demonstrate at low heat fluxes of below around 3×10^4 Wm^{-2} that the boiling curves of all test surfaces vary similarly with heat flux except for the cases of L=4mm. As the heat flux is raise, the overall heat transfer coefficients of most finned surfaces increase to a maximum value and then decrease as the heat flux is raised further. This behavior can be explained as the increase in the active nucleate density with the wall temperature, until large clusters and accumulations of vapor form among the fins. After the peak value, the overall heat transfer coefficients begin to decay because of the increase in departure bubble resistance. However, the case with L=4mm in Figure 4.10 and 4.11 behave differently and its overall heat transfer coefficient is independent of heat flux. This particular behavior may be due to the suppression of departure bubble by long fin length. Moreover, the premature decline in overall heat transfer coefficients is noted in Figure 4.9, 4.10 and 4.11 for high fin length arrangements, and similar trends are also observed by Guglielmini[40] and Rainey[15].

It is also noted that all curves in Figure 4.9, 4.10 and 4.11 have almost the same overall heat transfer coefficients in low heat flux region. Figure 4.12 re-plot the overall heat transfer

coefficients versus the overall heat flux for twelve test surfaces before overall heat transfer coefficient begin to decline or level-off. The plots in Figure 4.12 show that all experimental data lie on a straight line which can be correlated in a linear equation form:

$$h_t = 5.781 q_t''^{0.619} \tag{4-4}$$

Eq. (4-4) can also be written in term of the power law written as a simplified Roshsenow's [55] correlation:

$$q_t'' = 100 \Delta T^{2.625} \tag{4-5}$$

which shows strongly the dependence on the wall superheat.

Historically, the exponent on ΔT has been taken to be about 3 for nucleate boiling (Rohsenow [55]). The exponent of 3 on ΔT indicates that the primary heat transfer mode before the overall heat transfer coefficient begin to decline or level-off is nucleate boiling.

4.2.3 Heat transfer rate and CHF enhancement with area ratio and aspect ratio

Figure 4.13 plots the enhanced heat transfer ratio ($\dot{Q}_{f,CHF} / \dot{Q}_{p,CHF}$) versus the area ratio (A_t / A_b). The figure shows that $\dot{Q}_{f,CHF} / \dot{Q}_{p,CHF}$ increases with A_t / A_b as increasing the area increases the heat transfer. However, the plot also showed that $\dot{Q}_{f,CHF} / \dot{Q}_{p,CHF}$ is not always linearly proportional to A_t / A_b. In response of large increase in area, the enhancement of heat transfer rate decreases because increasing the area by increasing fin length or making fin closer increases flow resistance to departure vapor mushrooms.

Figure 4.13 also depicts $q_{f,CHF}'' / q_{p,CHF}''$ against A_t / A_b. It shows two distinct regions of enhancements - $q_{f,CHF}'' / q_{p,CHF}'' > 1$ and $q_{f,CHF}'' / q_{p,CHF}'' < 1$. A comparison with Table 4.2 shows that the plot of $q_{f,CHF}'' / q_{p,CHF}''$ corresponds to the fin aspect ratio ($\alpha = $L/S). In the region $q_{f,CHF}'' / q_{p,CHF}'' > 1$, the fin aspect ratios of the test surfaces are all less than or equal to 1. In the

region in which $q''_{f,CHF} / q''_{p,CHF} < 1$, the fin aspect ratios all exceed 1. Those results prove the flow pattern observation that lower aspect ratio fins with either lower fin length or larger fin spacing provide lower resistance to the departure bubbles and re-wetting liquid and yield higher heat transfer rate per unit area. The above analysis clearly shows that the fin aspect ratio strongly affects the CHF enhancement.

The two parameters that are found to affect CHF in the present data are: fin length and fin spacing. For the analysis of CHF behavior, the present mini-finned surfaces' CHF values that based on overall surface area are normalized by plain surface's CHF value. Figure 4.14 illustrates the mini-finned surface CHF behavior of the cases for all fin lengths and spacing. From Figure, it can be seen that the normalized CHF values ($q''_{t,CHF} / q''_{p,CHF}$) increase with increasing of dimensionless quantity (S/L). Between 0.125 and 1 of S/L, the normalized CHF values are raised significantly. This increase of enhancement can be ascribed to the fact that reducing the fin length or increasing the fin spacing can reducing the re-wetting liquid resistance from the fin blockage and departing bubbles, which effectively increase the dependency of CHF on surface structure. As can be seen from Figure, normalized CHF values in the high (S/L) region of 1 to 4 become relatively constant with values in a range of 1 to 1.2. This indicates that CHF values for the low profile mini-finned surfaces can be enhanced by convection mechanisms caused by the surface structure. From the plot in Figure 4.14, the normalized CHF values are correlated by the following equation:

$$q''_{t,CHF} / q''_{p,CHF} = 1.029(\frac{S}{L})^{0.178}$$
(4-6)

4.3 Conclusion Remarks

An experimental investigation of pool boiling phenomena for plain and finned surfaces immersed in saturated FC-72 at atmospheric pressure is presented in this chapter. The effects of geometric parameters on the nucleate boiling heat transfer performance with different fin

length and spacing are also reported. Analysis of the experimental results leads to the following conclusions:

1. Boiling generally initiates at the tip of the fin, whence it spreads to the fin root, regardless the wall superheat at the fin root exceed that of the fin tip. This result is associated with the fact that generated bubbles can be easily trapped at the fin root and eliminated by the convective flow.

2. A short periodical departure flow process is observed as heat flux approaches to CHF, where large vapor mushroom clouds are found to accumulate inside the fin spacing before splitting into several vapor clouds prior to lift-off.

3. Boiling incipience superheat drops as the fin length increases and the fin spacing decreases. The denser and higher fin array also eliminates the temperature excursion. Reducing the fin spacing and increasing the fin length also increase the flow resistance to bubble departure and also causes an early decline or level-off of the overall heat transfer coefficient.

4. Reducing the fin spacing or increasing the fin length can raise the heat transfer rate. The maximum heat transfer rate of the test surface with the smallest fin spacing and the highest fins is 98.3W almost five times that of the plain surface.

5. The enhancement of heat transfer rate is not linear proportion to the total area enhancement of the finned surface. Lower aspect ratio fins, either lower fin length or larger fin spacing, provide lower resistance to the departure bubble and re-wetting liquid and yield higher heat transfer rate per unit area.

6. It is believed that the presence of the mini-finned surface produces a resistance to vapor bubble departure, which increases the bubble residence time and causes a change in boiling curve slope of finned surfaces. The longer bubble residence time would also increase the flow resistance on the approaching re-wetting liquid causing liquid starvation and ultimately produce a temporal localized dry-out situation in the central portion of the fin array.

7. At low heat flux region, the finned surfaces show an appreciably higher overall heat transfer coefficient than the plain surface. In these conditions the heat transfer efficiency is quite similar for the various arrays of fins. At high heat flux region, fin spacing and length configuration appear to influence boiling heat transfer efficiency strongly.

Table 4.1 Average boiling incipience superheat of horizontal mini-finned surfaces.

Boiling Incipience superheat (K)	L=0.5mm	L=1.0mm	L=2.0mm	L=4.0mm
S=0.5mm	10.49	8.37	8.05	7.62
S=1.0mm	10.71	8.50	8.36	8.23
S=2.0mm	11.25	10.22	9.52	9.10

Table 4.2 Geometric parameters of mini-finned surfaces.

A_t/α	L=0.5mm	L=1.0mm	L=2.0mm	L=4.0mm
S=0.5mm	198mm^2/1	296 mm^2/2	492 mm^2/4	884 mm^2/8
S=1.0mm	150 mm^2/0.5	200 mm^2/1	300 mm^2/2	500 mm^2/4
S=2.0mm	132 mm^2/0.25	164 mm^2/0.5	228 mm^2/1	356 mm^2/2

α : aspect ratio of fin spacing
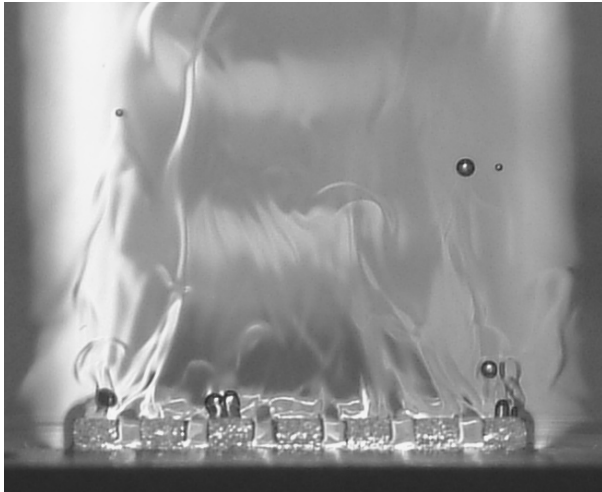
(a) S=0.5mm, L=0.5mm, 2.6% of CHF   (b) S=0.5mm, L=1.0mm, 2.0% of CHF
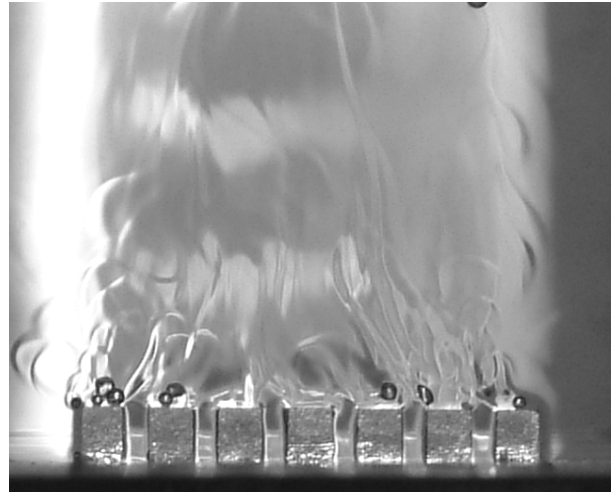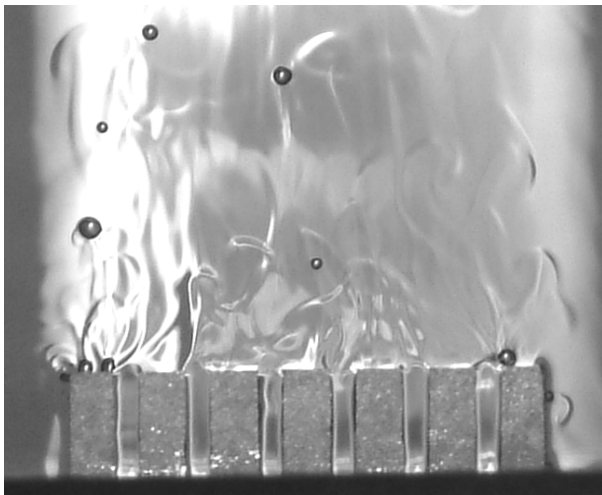
(c) S=0.5mm, L=2.0mm, 1.5% of CHF   (d) S=0.5mm, L=4.0mm, 1.2% of CHF
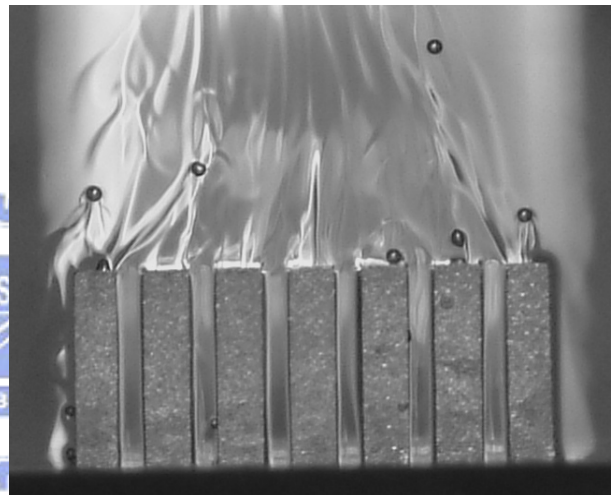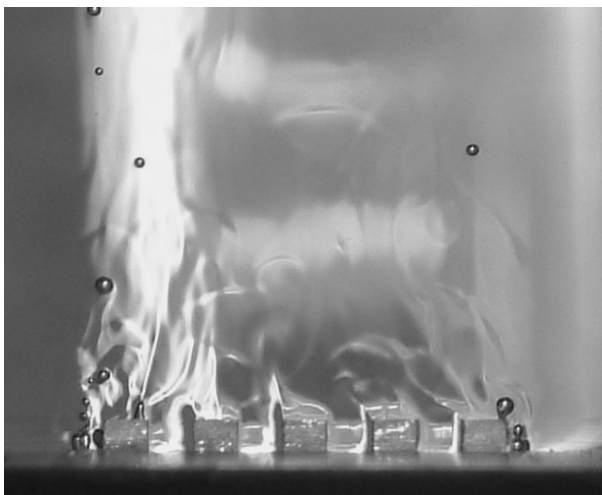
(e) S=1.0mm, L=0.5mm, 3.5% of CHF   (f) S=1.0mm, L=1.0mm, 2.7% of CHF
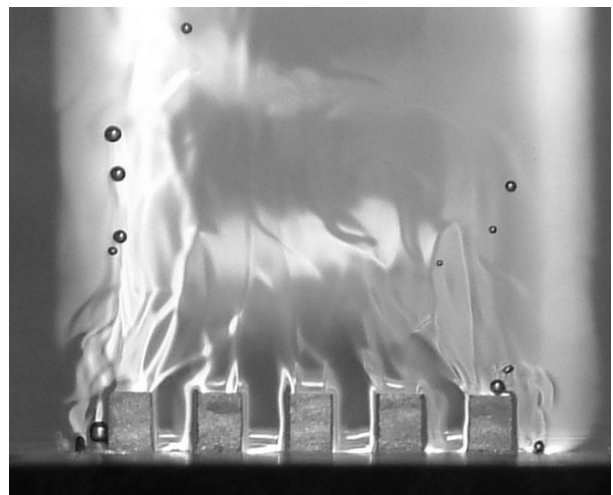
Figure 4.1 Flow patterns of 12 mini-finned surfaces at boiling incipience.

continued
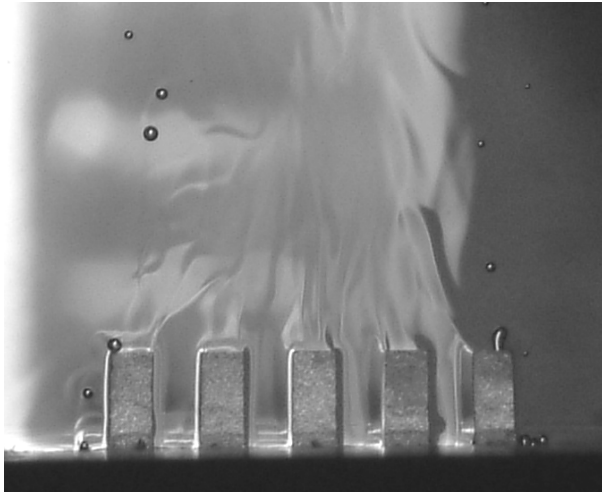
(g) S=1.0mm, L=2.0mm, 1.9% of CHF   (h) S=1.0mm, L=4.0mm, 2.5% of CHF
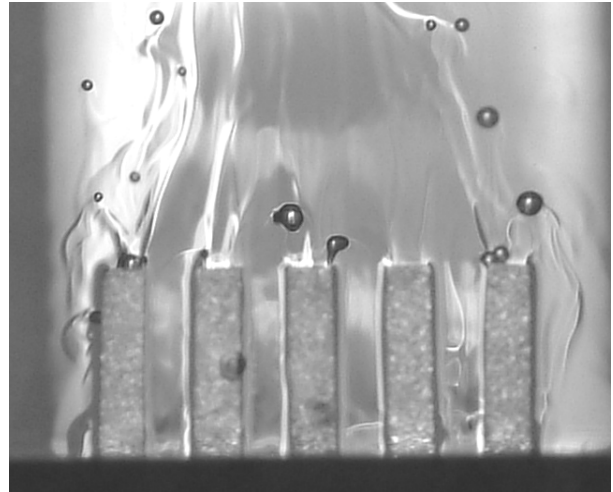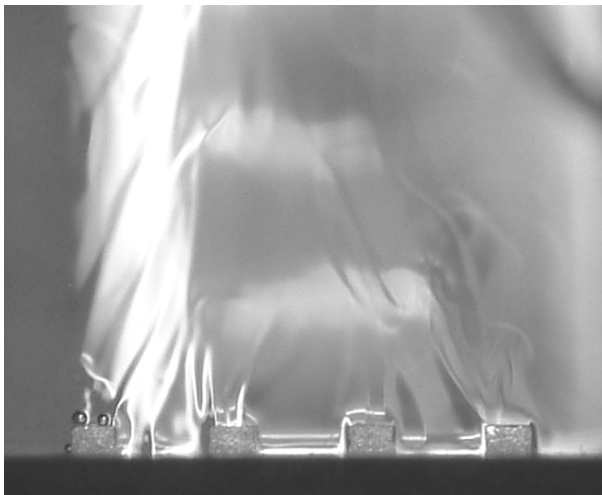
(i) S=2.0mm, L=0.5mm, 3.3% of CHF   (j) S=2.0mm, L=1.0mm, 2.8% of CHF
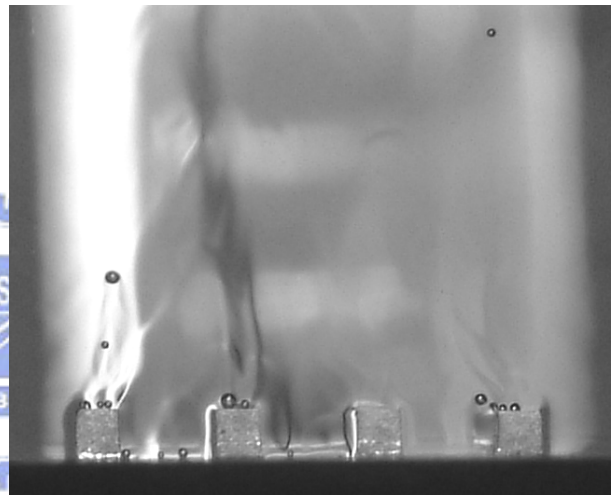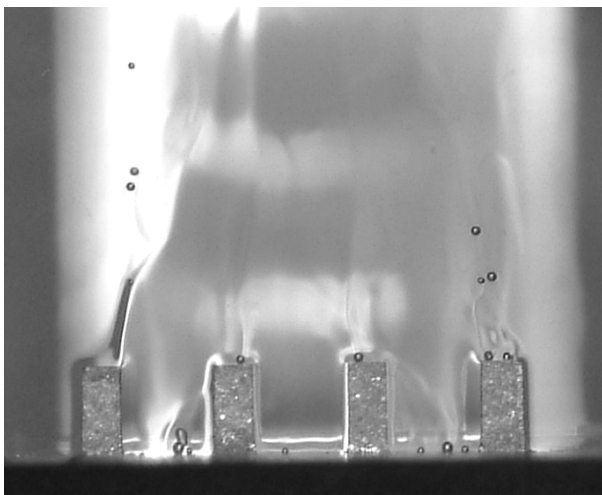
(k) S=2.0mm, L=2.0mm, 2.2% of CHF   (l) S=2.0mm, L=4.0mm, 1.5% of CHF
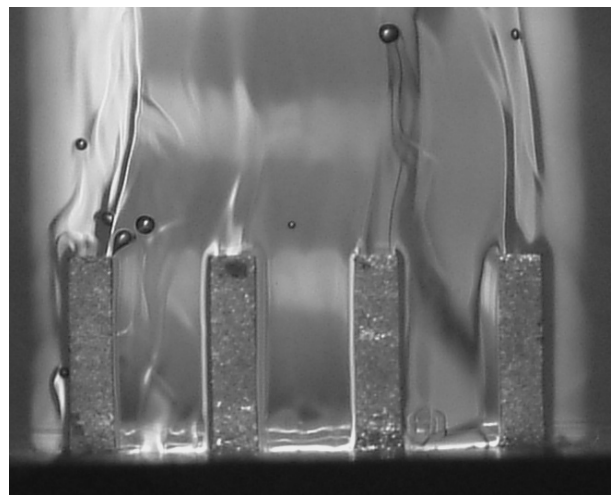
Figure 4.1 Flow patterns of 12 mini-finned surfaces at boiling incipience.
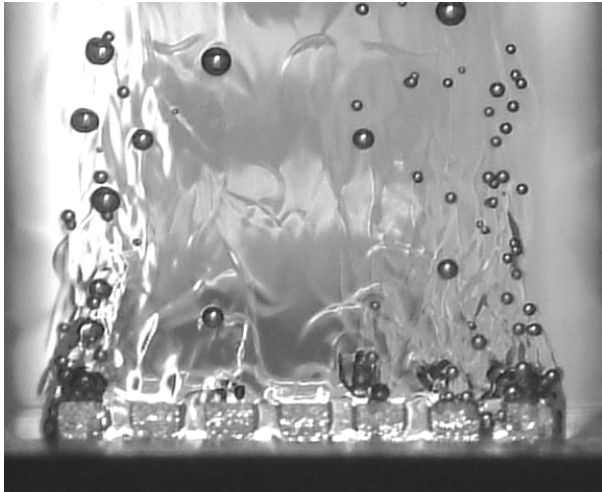
(a) S=0.5mm, L=0.5mm, 23.1% of CHF
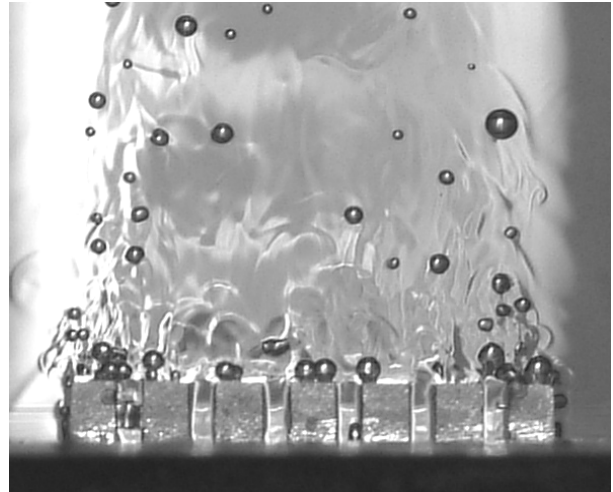
(b) S=0.5mm, L=1.0mm, 22.8% of CHF
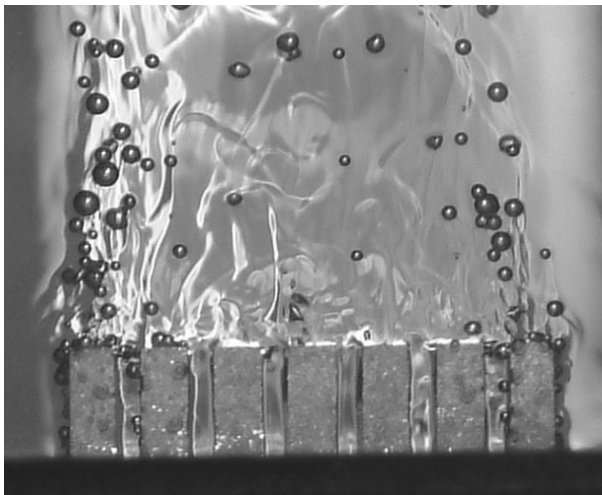
(c) S=0.5mm, L=2.0mm, 24.5% of CHF
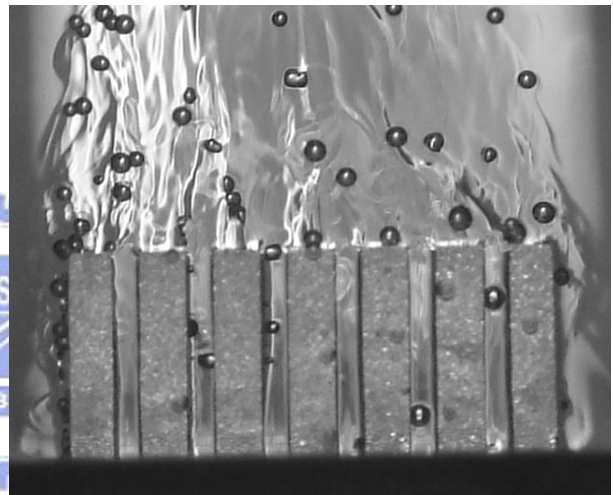
(d) S=0.5mm, L=4.0mm, 22.3% of CHF
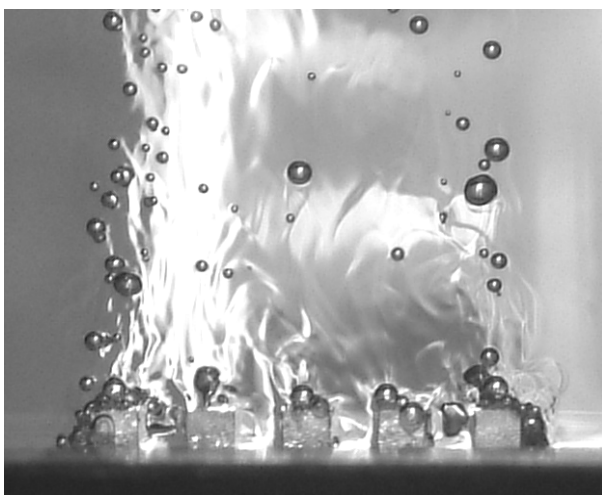
(e) S=1.0mm, L=0.5mm, 22.8% of CHF
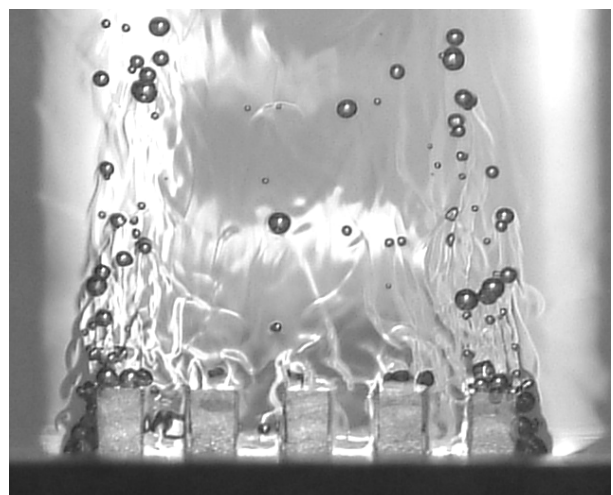
(f) S=1.0mm, L=1.0mm, 23.3% of CHF

Figure 4.2 Flow patterns of 12 mini-finned surfaces at low heat flux region.

continued
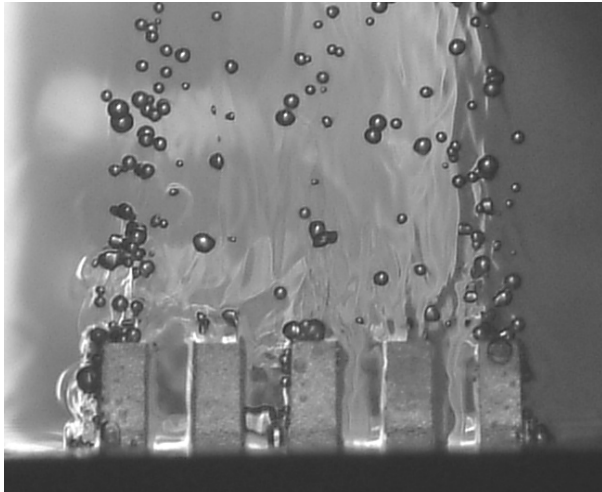
(g) S=1.0mm, L=2.0mm, 24.6% of CHF
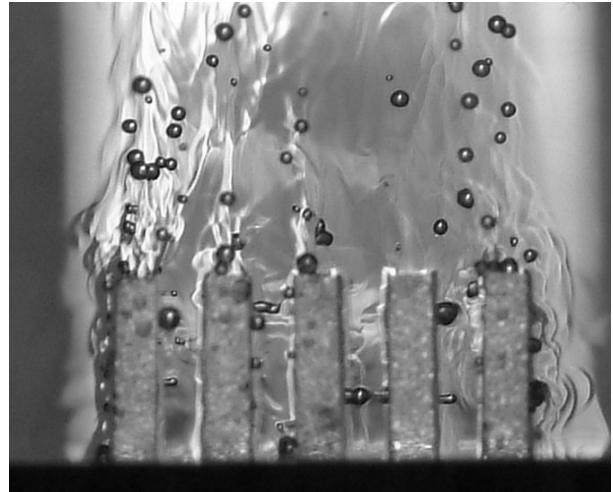
(h) S=1.0mm, L=4.0mm, 22.1% of CHF
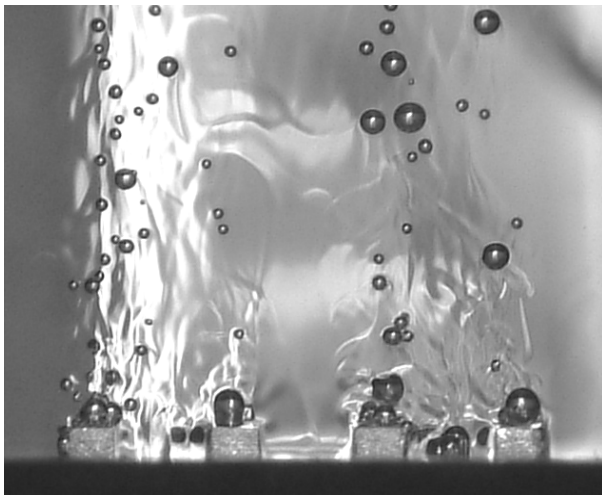
(i) S=2.0mm, L=0.5mm, 24.5% of CHF

(j) S=2.0mm, L=1.0mm, 22.9% of CHF
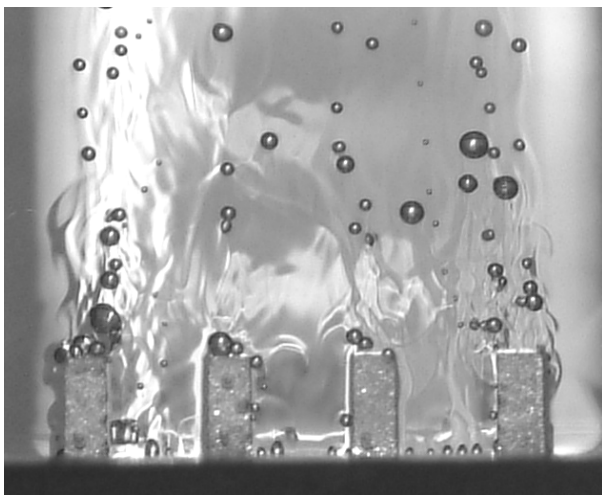
(e) S=2.0mm, L=2.0mm, 22.6% of CHF
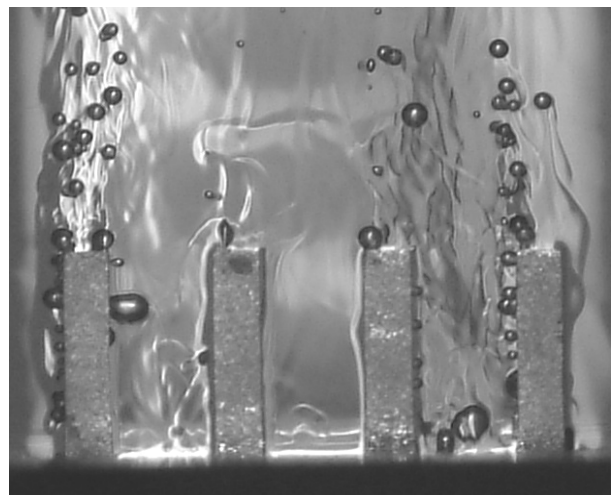
(f) S=2.0mm, L=4.0mm, 23.5% of CHF

Figure 4.2 Flow patterns of 12 mini-finned surfaces at low heat flux region.
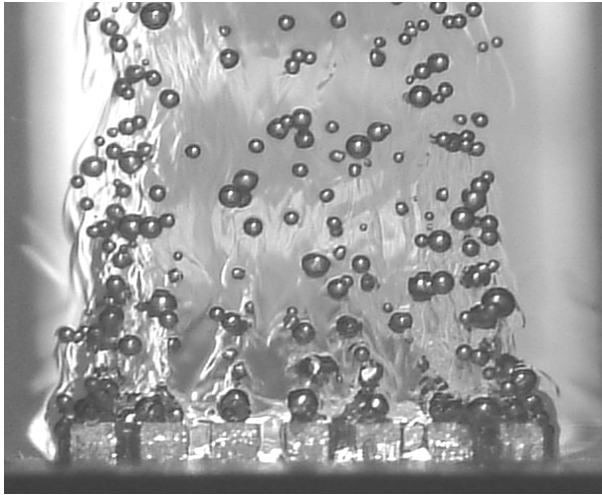
(a) S=0.5mm, L=0.5mm, 58.9% of CHF (b) S=0.5mm, L=1.0mm, 56.1% of CHF
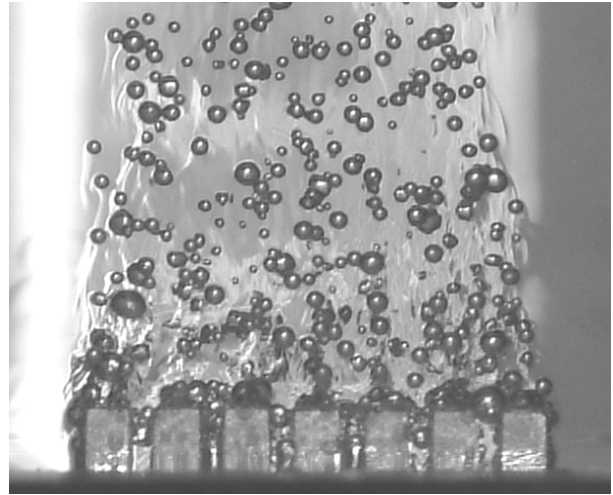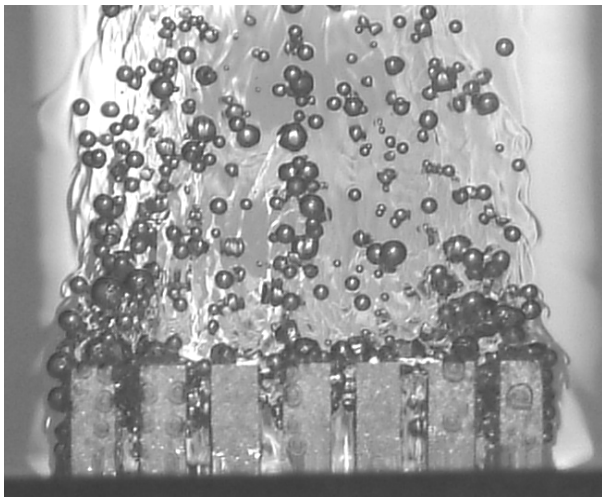
(c) S=0.5mm, L=2.0mm, 57.3% of CHF (d) S=0.5mm, L=4.0mm, 56.8% of CHF
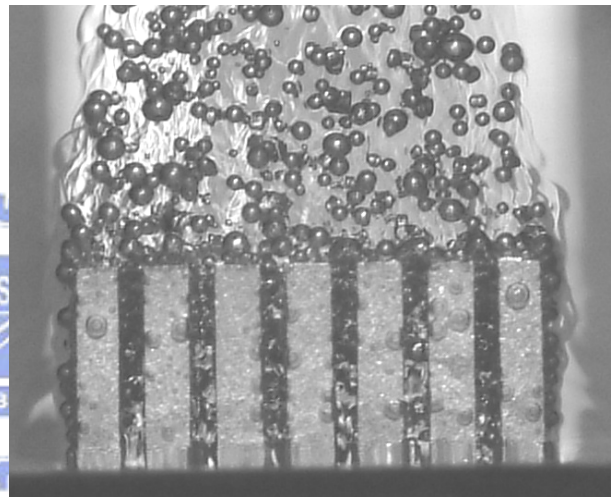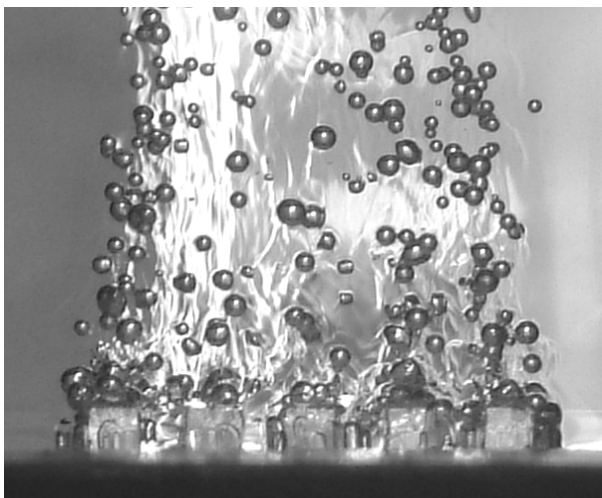
(e) S=1.0mm, L=0.5mm, 57.5% of CHF (f) S=1.0mm, L=1.0mm, 56.1% of CHF
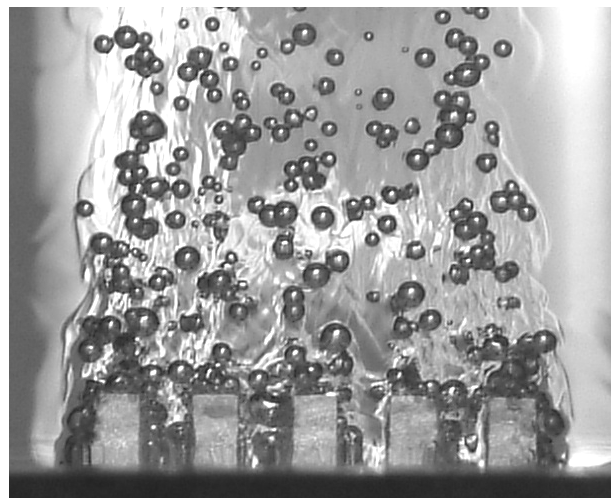
Figure 4.3 Flow patterns of 12 mini-finned surfaces at moderate heat flux region.

continued
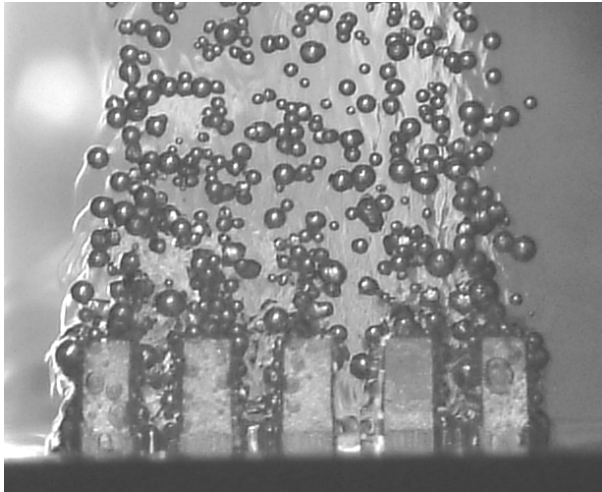
(g) S=1.0mm, L=2.0mm, 57.6% of CHF
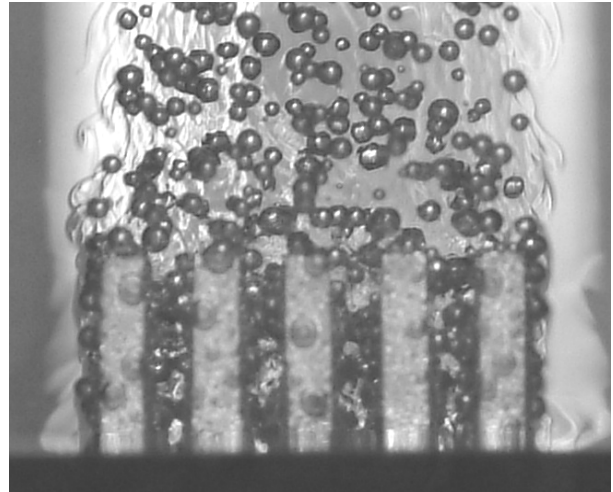
(h) S=1.0mm, L=4.0mm, 57.3% of CHF
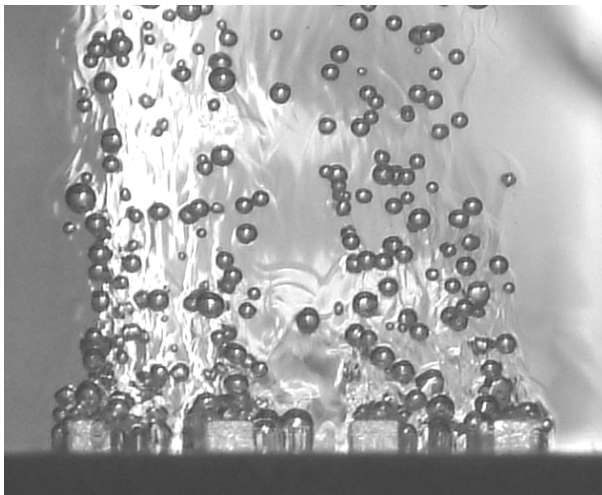
(i) S=2.0mm, L=0.5mm, 56.6% of CHF
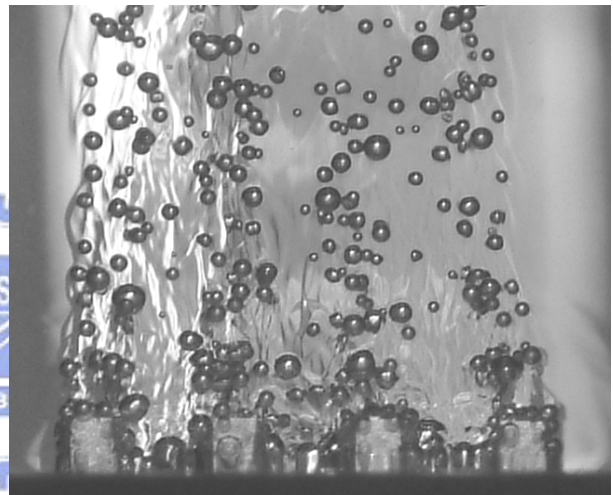
(j) S=2.0mm, L=1.0mm, 57.4% of CHF
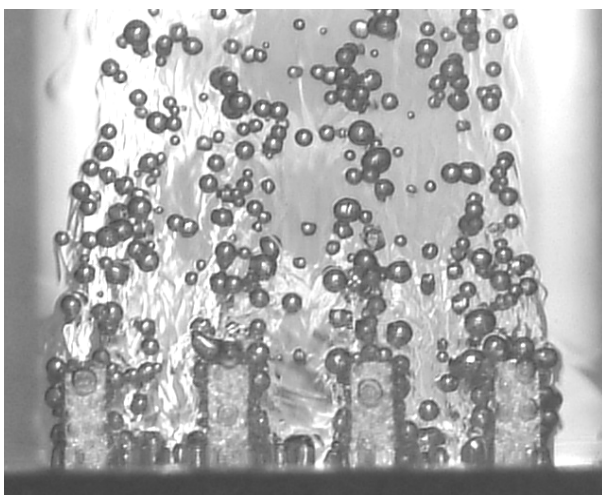
(k) S=2.0mm, L=1.0mm, 55.7% of CHF
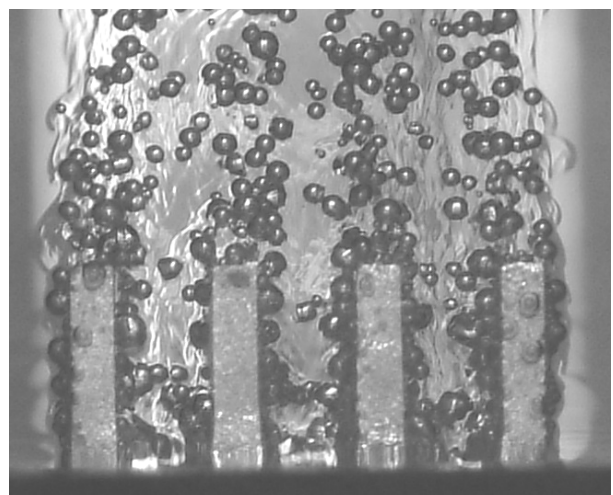
(l) S=2.0mm, L=4.0mm, 58.3% of CHF

Figure 4.3 Flow patterns of 12 mini-finned surfaces at moderate heat flux region.
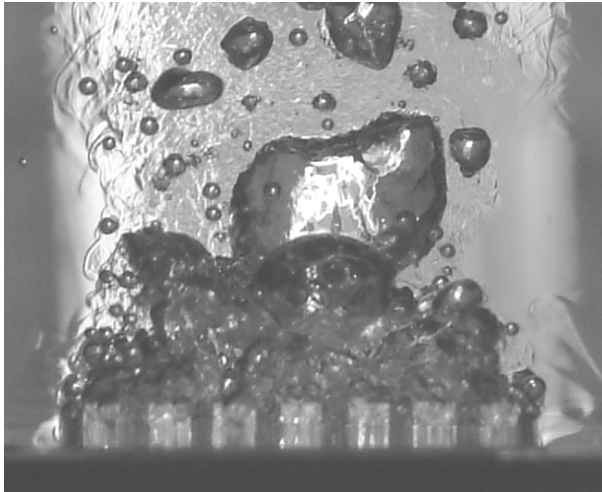
(a) S=0.5mm, L=0.5mm, 84.7% of CHF
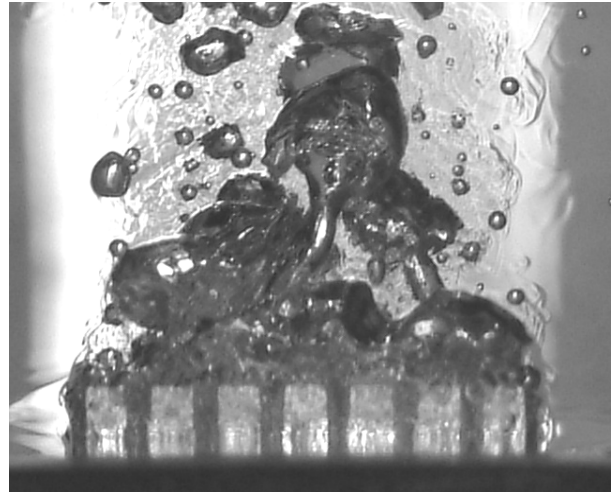
(b) S=0.5mm, L=1.0mm, 82.2% of CHF
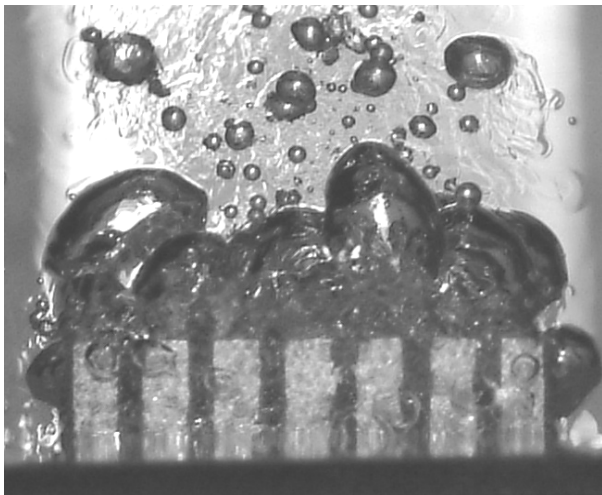
(c) S=0.5mm, L=2.0mm, 85.6% of CHF
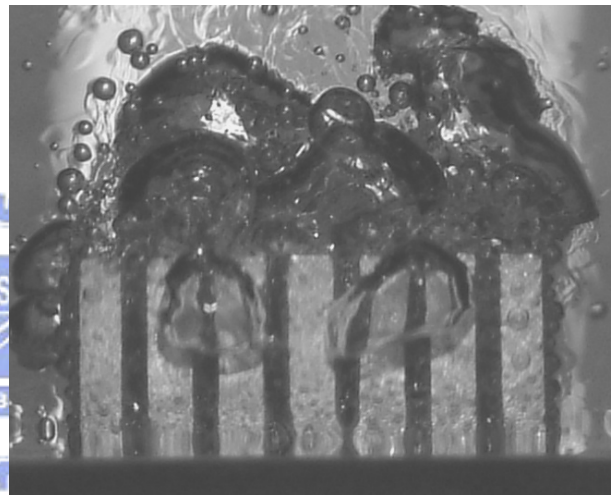
(d) S=0.5mm, L=4.0mm, 81.3% of CHF
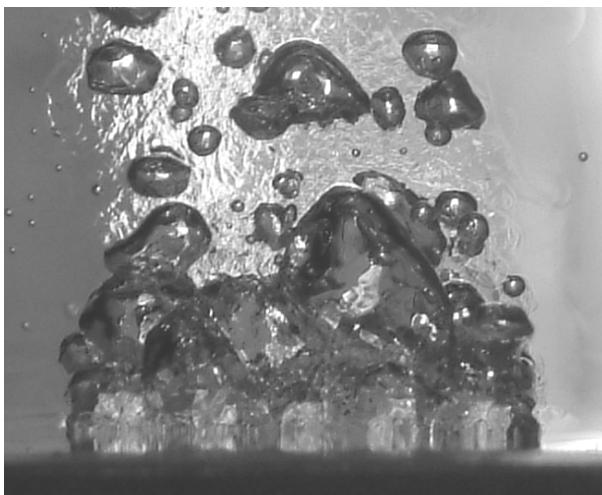
(e) S=1.0mm, L=0.5mm, 82.7% of CHF
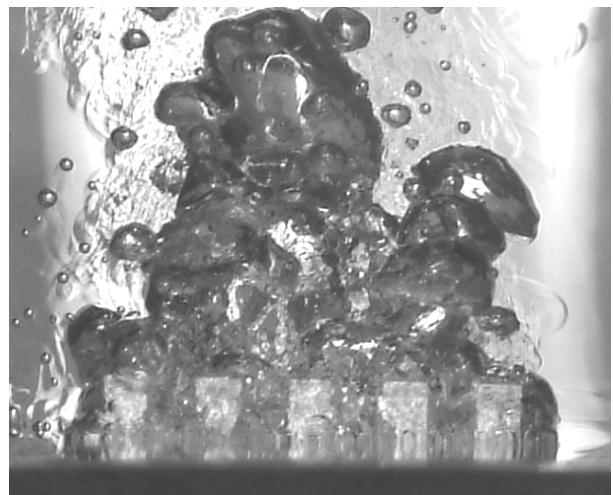
(f) S=1.0mm, L=1.0mm, 85.2% of CHF

Figure 4.4 Flow patterns of 12 mini-finned surfaces at high heat flux region approach to CHF.
continued
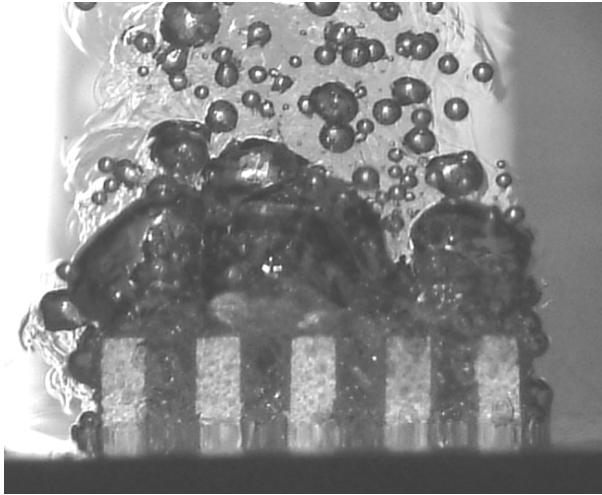
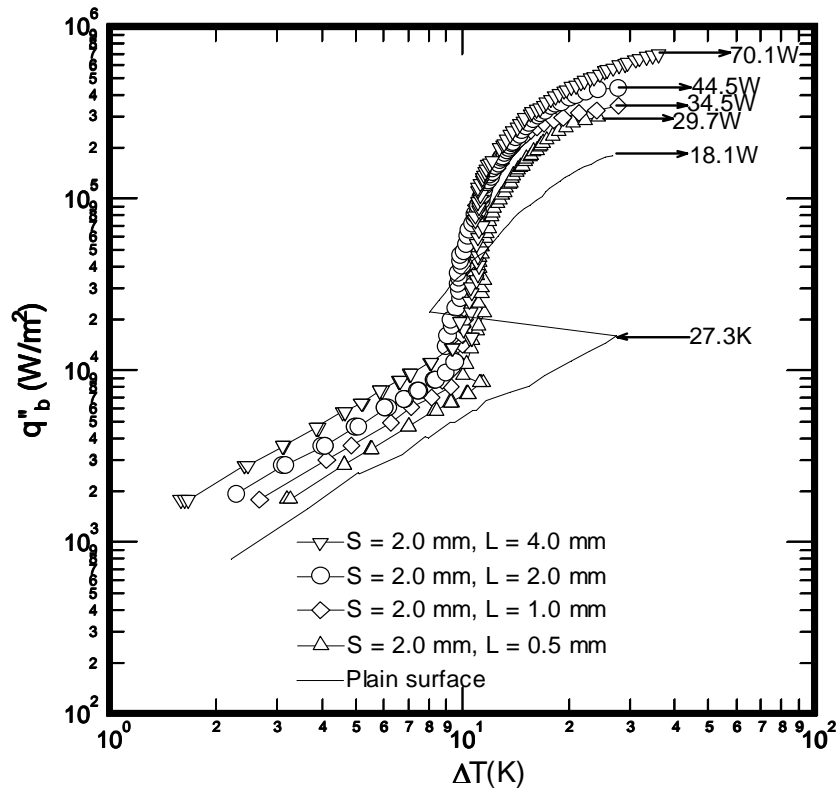(g) S=1.0mm, L=2.0mm, 84.3% of CHF
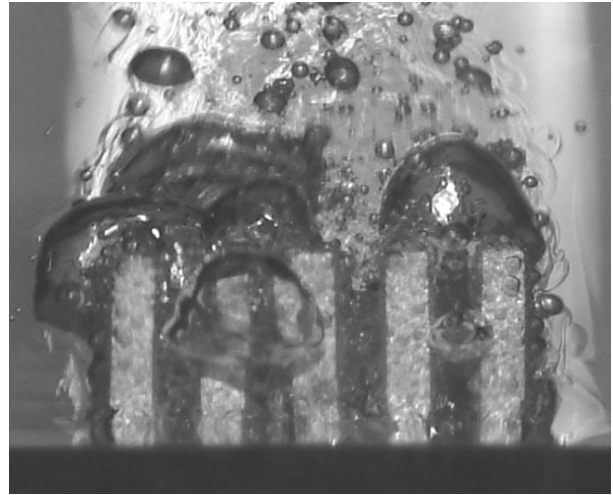
(h) S=1.0mm, L=4.0mm, 84.9% of CHF
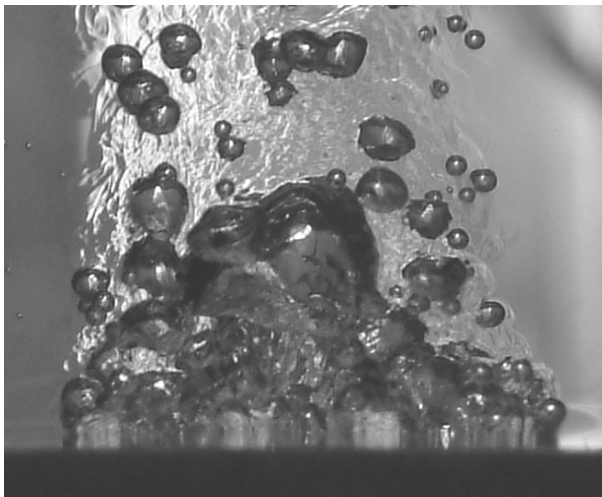
(i) S=2.0mm, L=0.5mm, 84.5% of CHF
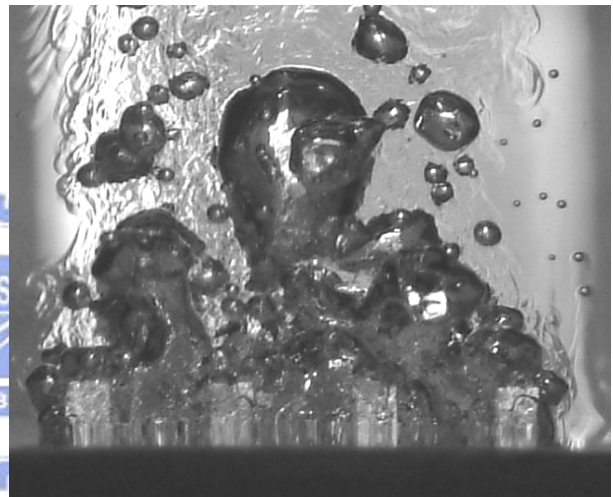
(j) S=2.0mm, L=1.0mm, 82.6% of CHF
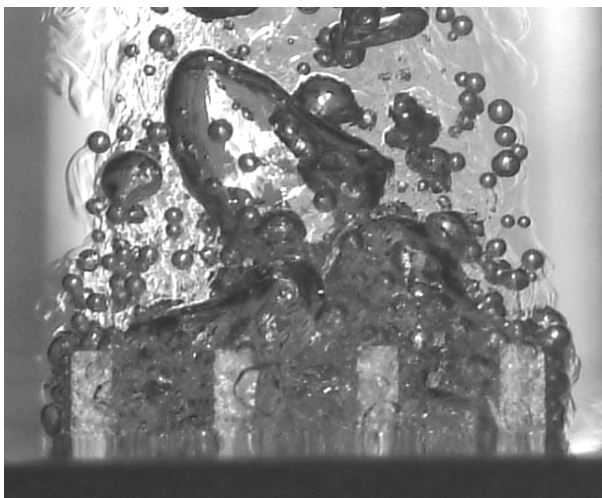
(k) S=2.0mm, L=2.0mm, 81.3% of CHF
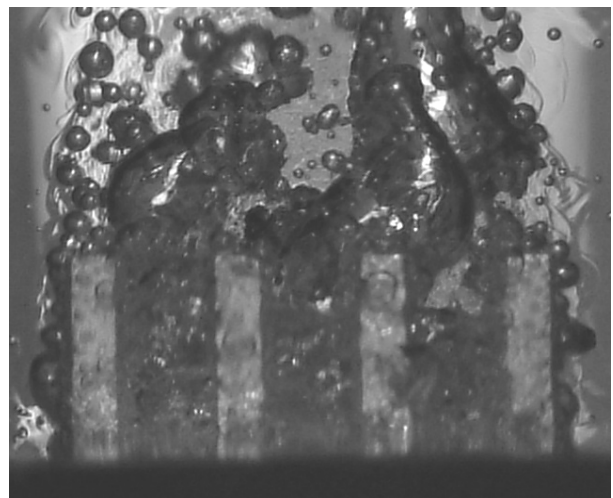
(l) S=2.0mm, L=4.0mm, 83.8% of CHF

Figure 4.4 Flow patterns of 12 mini-finned surfaces at high heat flux region approach to CHF.

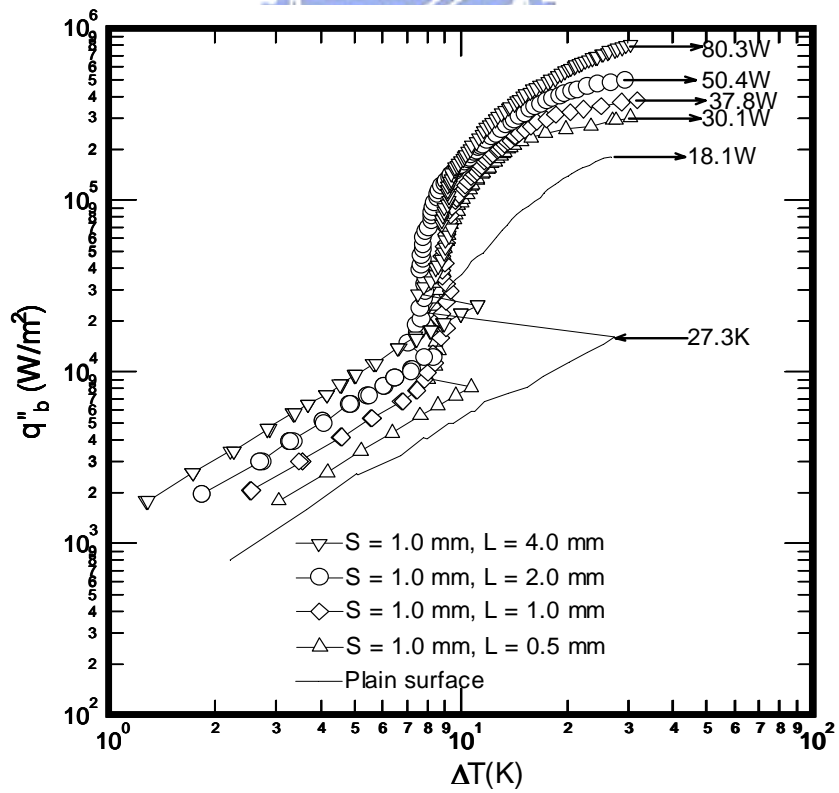Figure 4.5 Boiling curves of mini-finned surface with various fin length (S=2.0mm, increasing heat flux).

Figure 4.6 Boiling curves of mini-finned surface with various fin length (S=1.0mm, increasing heat flux).
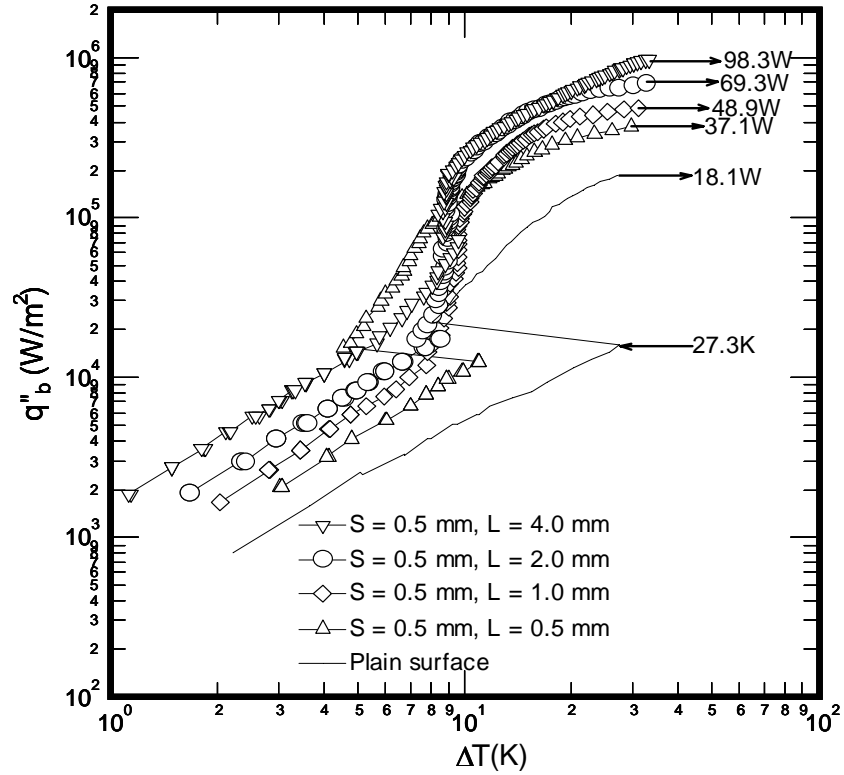
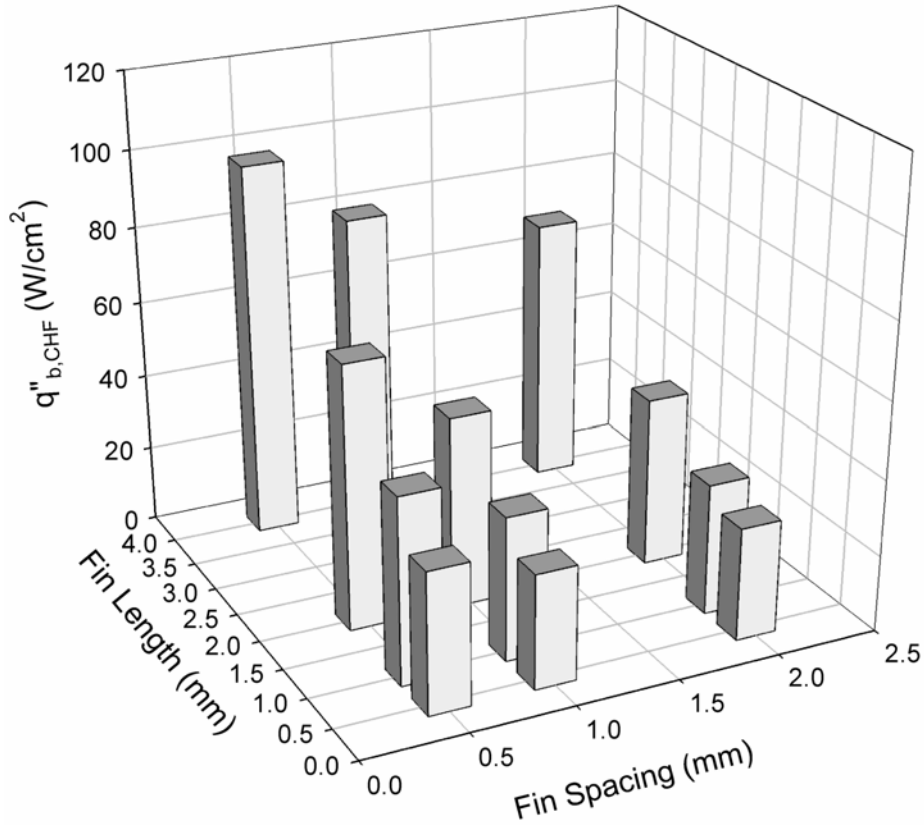Figure 4.7 Boiling curves of mini-finned surface with various fin length (S=0.5mm, increasing heat flux).

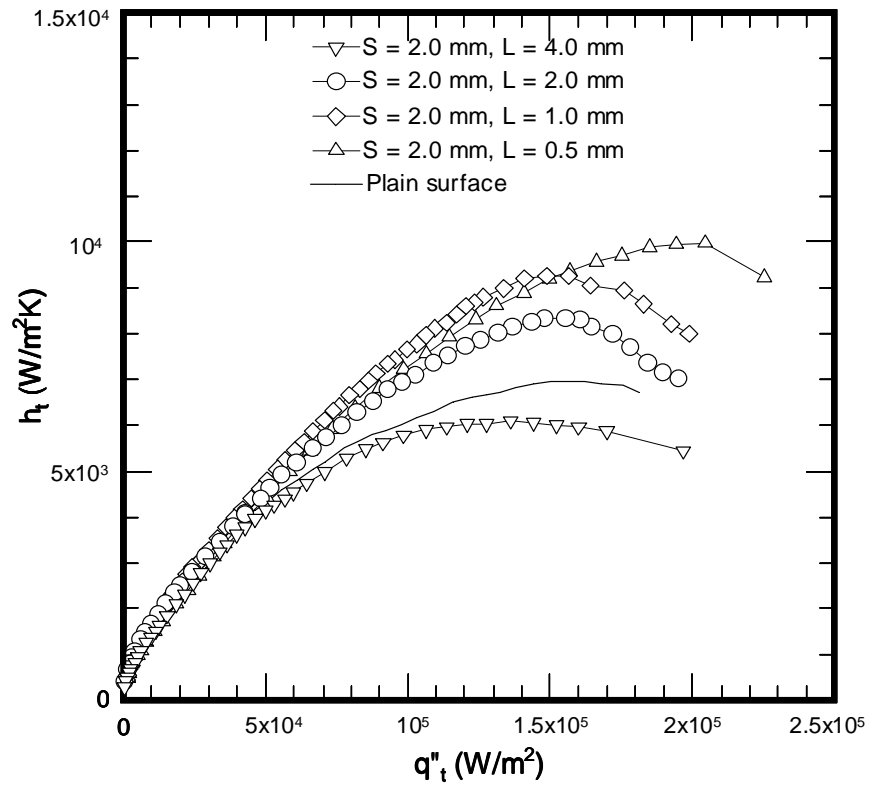Figure 4.8 Critical heat flux ($q''_{b,CHF}$) varied with fin spacing and length.

Figure 4.9 Variations of overall heat transfer coefficient with overall heat flux for various fin length (S=2.0mm, decreasing heat flux).
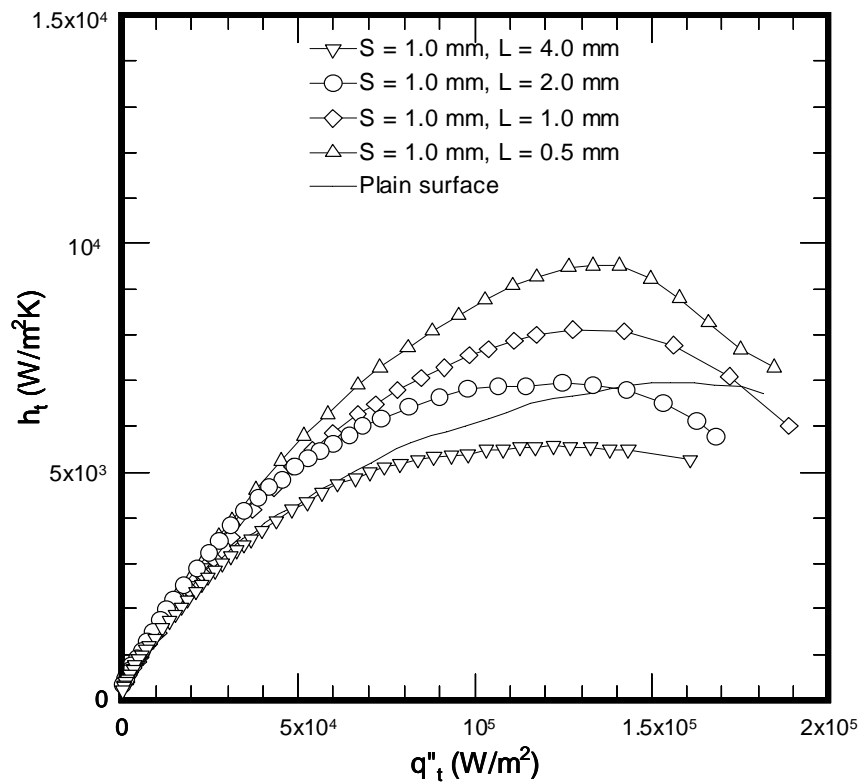

Figure 4.10 Variations of overall heat transfer coefficient with overall heat flux for various fin length (S=1.0mm, decreasing heat flux).
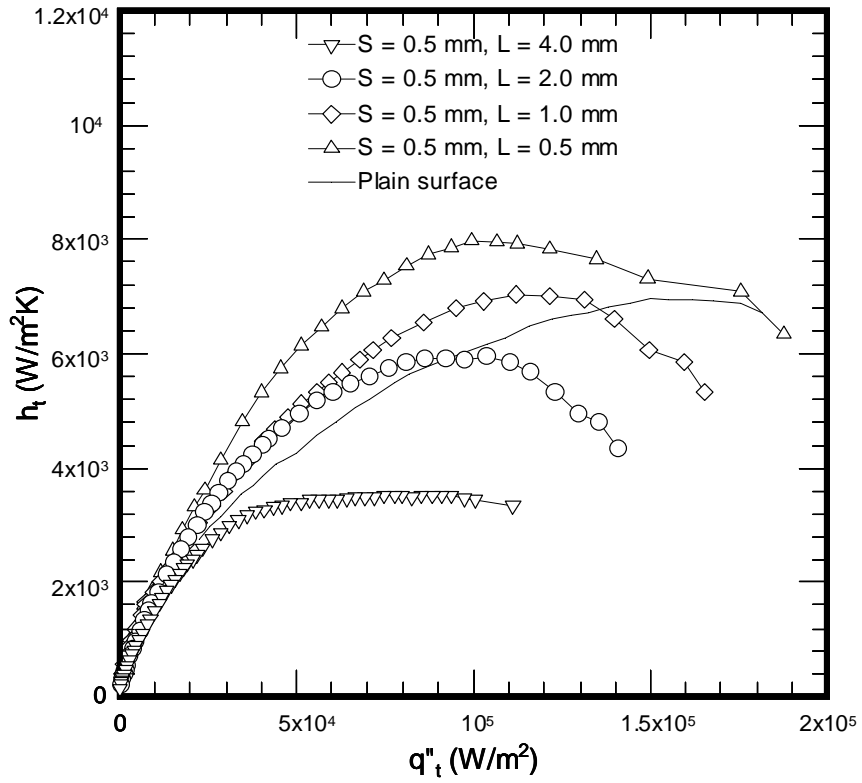
68

Figure 4.11 Variations of overall heat transfer coefficient with overall heat flux for various fin length (S=0.5mm, decreasing heat flux).
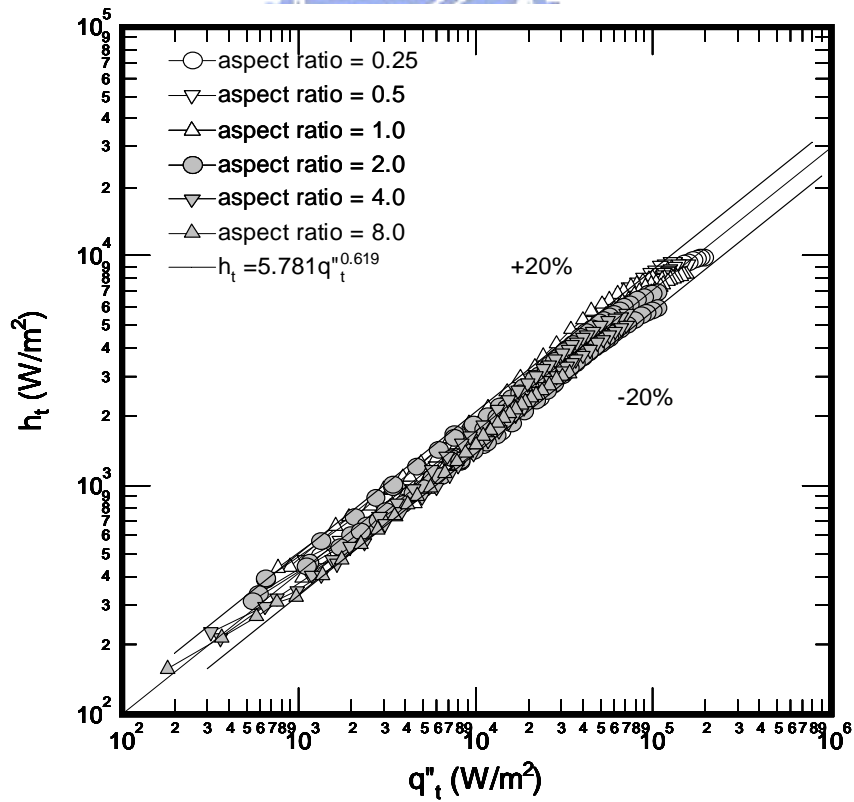

Figure 4.12 Overall heat transfer coefficients versus overall heat flux for different finned surfaces.
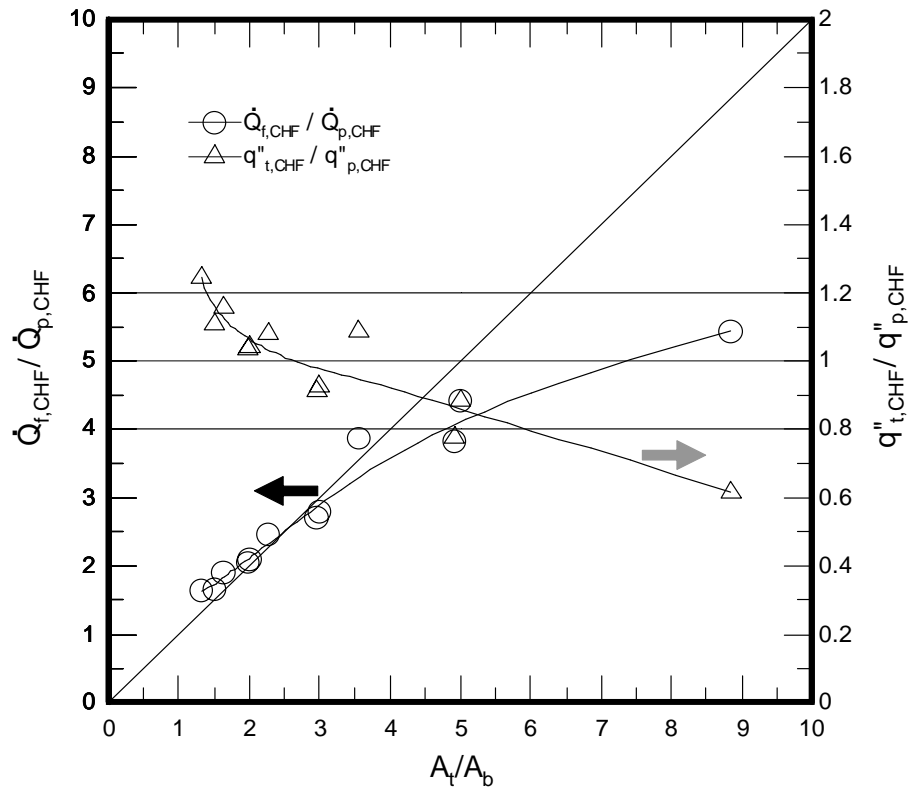
Figure 4.13 Enhancement of maximum heat rate and critical heat flux versus enhancement of area.
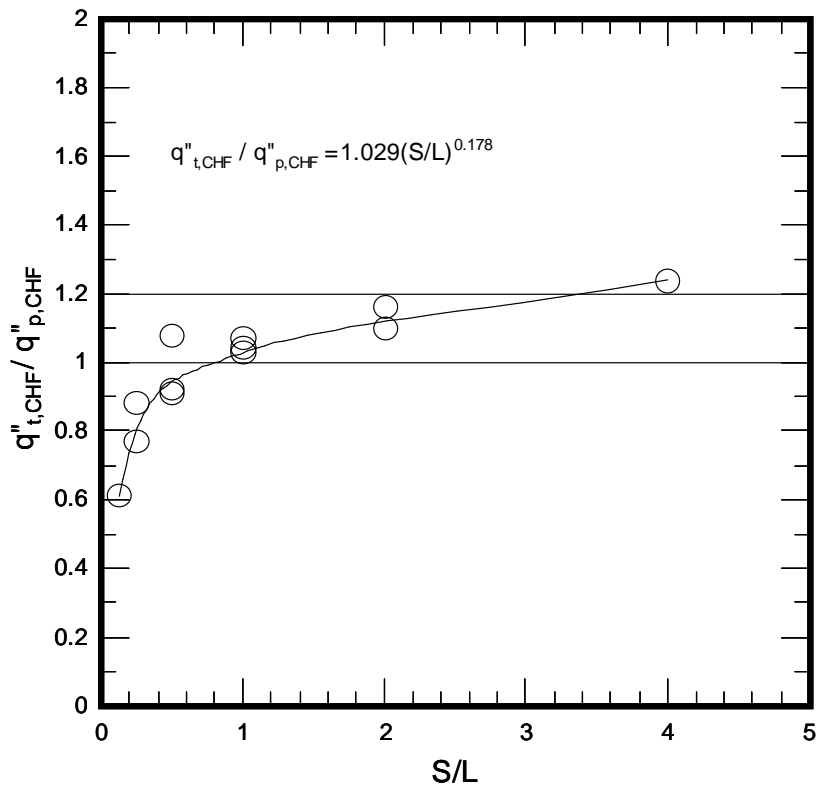

Figure 4.14 Normalized overall heat fluxes versus dimensionless parameter (S/L).